John F. Schenck, MD, PhD • Ferenc A. Jolesz, MD • Peter B. Roemer, PhD[2] • Harvey E. Cline, PhD
William E. Lorensen, MS • Ronald Kikinis, MD • Stuart G. Silverman, MD • Christopher J. Hardy, PhD
William D. Barber, MS • E. Trifon Laskaris, PhD • Bijan Dorri, PhD • Robert W. Newman, MS
Catherine E. Holley, RN • Bruce D. Collick, PhD • Douglas P. Dietz, MID, • David C. Mack, MS
Maureen D. Ainslie, BS, RT • Patrick L. Jaskolski, BS • Michael R. Figueira, MS • John C. vom Lehn, MS
Steven P. Souza, PhD • Charles L. Dumoulin, PhD • Robert D. Darrow, MS • Richard L. St. Peters, PhD
Kenneth W. Rohling • Ronald D. Watkins • David R. Eisner • S. Morry Blumenfeld, PhD
Kirby G. Vosburgh, PhD

Superconducting Open-Configuration MR Imaging System for Image-guided Therapy[1]

PURPOSE: **To develop a superconducting magnetic resonance (MR) imager that provides direct access to the patient and permits interactive MR-guided interventional procedures.**

MATERIALS AND METHODS: **A 0.5-T superconducting magnet that allows a region of vertical access to the patient was designed and constructed. This magnet was integrated with newly designed shielded gradient coils, flexible surface coils, and nonmagnetic displays and with position-monitoring probes and device-tracking instrumentation.**

RESULTS: **The magnet homogeneity was 12.3 ppm, and the gradient field was linear to within 1% over an imaging region 30 cm in diameter. The signal-to-noise ratio was 10% higher than in a comparable 0.5-T superconducting imager. Images were obtained in several anatomic regions with use of routine pulse sequences. Interactive image plane selection and near real-time imaging, with use of fast gradient-recalled echo sequences, were demonstrated at a rate of one image every 1.5 seconds.**

CONCLUSION: **MR-guided interventional procedures can be performed with full patient access with use of an open-configuration, superconducting MR magnet with near real-time imaging and interactive image plane control.**

Index terms: Interventional procedures, technology • Magnetic resonance (MR), guidance

Radiology 1995; 195:805–814

There has recently been a great interest in expanding the scope of image-guided, invasive therapeutic procedures (1). Magnetic resonance (MR) imaging provides excellent tissue discrimination, and its capability for tissue targeting and localization has been widely used for the guidance of biopsy and stereotaxic procedures (2–17). In addition, near real-time MR imaging monitoring and control are useful for interventional procedures such as interstitial laser photocoagulation (8–29), cryotherapy (30,31), and focused ultrasound (US) (32–37) that use thermal energy for the ablation of diseased tissues. The emergence of minimally invasive interventional procedures (such as endovascular, endoscopic, laparoscopic) as an alternative to conventional surgical procedures (38) motivates the development of strategies for three-dimensional image guidance that are more efficient and better integrated with therapeutic devices than are the fluoroscopic, computed tomographic (CT), and US systems currently in use.

However, technical barriers, particularly the inaccessibility of the patient during the imaging process, have prevented the widespread use of conventional, superconducting MR imagers for intraoperative guidance. This has prompted us to develop a new, open-configuration, superconducting MR imaging system, which allows direct access to the patient during the execution of treatment protocols. This system permits the acquisition of high quality, near real-time MR images under the direct control of the interventional radiologist, who can perform such procedures while standing or seated within the magnet itself.

The goal of this project was the development of new and less invasive procedures based on intraoperative MR imaging guidance. Beside the conventional MR imaging contrast mechanisms, these procedures can use the direct sensitivity of MR imaging to tissue temperature and the sensitivity to temperature-induced biochemical changes, such as protein denaturation and coagulation necrosis.

MR imaging requires a strong, static magnetic field that is highly uniform over the imaging field of view (FOV) (39). Several magnet configurations that produce these fields are in use (Table 1). For superconducting systems, field uniformity is achieved by using a set of cylindrically symmetric coils that are housed within a tubular cryostat, which fits rather tightly around the patient. This configuration precludes effective visual and manual contact with the area of the patient being imaged, which must be near the center of the imager. Also, the conventional, cylindrical configuration provides only a limited ability to observe and monitor anesthetized patients. Many of the MR imaging–assisted interventional procedures so far reported involve the use of images obtained before and after the procedure, and this does not permit real-time intraoperative monitoring. Other reported procedures involve interventions accomplished outside the magnet with the patient episodically moved into the imager for imaging purposes. The delays involved in moving a patient into and out of the magnet and the inaccessibility of the

---

[1] From the General Electric Corporate Research and Development Center, General Electric Co, Bldg K1/NMR, Schenectady, NY 12309 (J.F.S., P.B.R., H.E.C., W.E.L., C.J.H., W.D.B., E.T.L., B.D, J.C.v.L., S.P.S., C.L.D., R.D.D., R.L.St.P., K.W.R, R.D.W., D.R.E., K.G.V.); GE Medical Systems, Waukesha, Wis (R.W.N., B.D.C., D.P.D., D.C.M., P.L.J., M.R.F., S.M.B.); and the Department of Radiology, Brigham and Women's Hospital, Boston, Mass (F.A.J., R.K., S.G.S., C.E H., M.D.A.). Received June 6, 1994; revision requested August 5; revision received January 23, 1995; accepted February 14. **Address reprint requests to** J.F.S.

[2] Current address: Advanced NMR Systems, Wilmington, Mass.

Abbreviations: FOV = field of view, GRE = gradient-recalled echo, RF = radio frequency, S/N = signal-to-noise ratio.

patient during the imaging process limit the nature and scope of these procedures.

MR imagers that use a permanent magnet (39–41) or an electromagnet achieve a uniform static field with placement of the patient between two large magnetic pole faces. This type of imager permits a degree of patient access through the gap between the pole faces that is approximately 35 cm in most designs. Although this is not a physical requirement, the available MR imagers with a permanent magnet use horizontal pole faces, and the resulting patient access is in the horizontal plane. Vertical access from above the patient is not possible in this permanent-magnet configuration because of the presence of the pole faces. Imagers that use permanent magnets or electromagnets have lower field strengths (typically 0.05–0.2 T) than do superconducting systems (typically 0.5–1.5 T). The available signal-to-noise ratio (S/N) of MR imagers increases linearly with increasing field strength (39), thus giving imagers with a higher field strength the advantages of spatial and temporal resolution. The open-configuration imager described herein was developed to evaluate the potential advantages of vertical-access imagers that operate at superconducting field strengths.

It is desirable for the clinician to have interactive control of the imaging process during the procedure to permit rapid tissue targeting and visualization of dynamically changing anatomic relationships. The system described in this article provides continuous monitoring of the position of instruments, such as biopsy needles, forceps, catheters, and endoscopes, with the use of small optical and/or radio-frequency (RF) sensors mounted on the instruments. This information is used by a computer workstation that controls the imager, permitting the operator to perform multiplanar imaging at desired locations.

Table 1
Patient Accessibility during MR Imaging

Magnet Type	Magnetic Field Source	Patient Accessibility	Field Strength (T)
Conventional superconducting magnet	Superconducting coils in a cylindrical cryostat	Inaccessible	0.5–1.5
Permanent magnet	Horizontal, magnetized pole faces	Horizontal access	0.05–0.2
Open-configuration superconducting magnet	Superconducting coils in a split cryostat with a region of central access	Vertical access	0.5

MATERIALS AND METHODS

The image console and electronics of a conventional MR imager (Signa; GE Medical Systems, Milwaukee, Wis) were used in conjunction with a new magnet, patient table, and gradient coils designed and built specifically for this application. The superconducting magnet (42) was designed with the coils in separate but communicating cryostats to achieve a spherical imaging volume 30 cm in diameter, with a 56-cm gap at the center of the magnet to permit vertical access to the patient (Figs 1, 2). As with most superconducting magnets, the coil location was a modification of that used in the traditional two-coil Helmholtz pair (39); however, the two-coil Helmholtz pair has a relatively narrow separation between the two coils (equal to the coil radius), and the region of homogeneity is too small for practical imaging purposes. Computer analysis of various coil designs was used to simultaneously optimize magnet-stored energy, the access gap between the innermost coils, and the volume of the highly homogeneous magnetic field over which MR imaging is possible. It was found that a six-coil configuration provided a sufficient number of degrees of freedom to achieve a satisfactory design.

The magnet was constructed at the General Electric Corporate Research and Development Center, Schenectady, NY. The inductance was 464 H, and the central field was 0.0077 T per ampere of coil current. The magnet weighed 3,600 kg and had an outer diameter of 1.84 m and a length of 1.48 m. If the magnet was unshielded, the 5-G (0.0005 T) line was at 10.0 m from the magnet center along the axis and 7.9 m transverse to the axis.

A superconducting material was used that permits an increase in the width of the region of access. Niobium tin, which has a superconducting transition temperature of 18.1 K, was used instead of the more common niobium titanium, which has a maximum superconducting transition temperature of 10.1 K (43). The high superconducting transition temperature of niobium tin permitted the coils to operate at temperatures above the approximately 4.2 K that is normally used. This made it possible to achieve sufficient cooling of the coils and thermal shield with use of a two-stage Gifford-McMahon cryocooler assembly (Kelcool UC130; Balzers, Hudson, NH), and no liquid helium was required. Because there was no helium bath, the spacing between the superconducting coils and the cryostat walls could be reduced, resulting in a wider zone of patient access.

The mechanical structure was designed to allow the magnet to operate safely at fields of up to 1 T, and the magnet has been successfully operated at fields up to 0.7 T. To achieve compatibility with standard imager components and to permit direct imaging comparisons with a standard 0.5-T MR imager (Signa Advantage; GE Medical Systems), an initial operating field of 0.5 T was chosen. This resulted in a peak field at the superconducting coils of 1.5 T. At 0.5 T, the magnet operated satisfactorily, with use of a single cryocooler, at a shield temperature of 13.2 K. However, to enhance the reliability, in normal operation, two cryocoolers were used and the shield temperature was maintained at 10 K. The superconducting coils were wound from superconducting tape (44,45) that was 3 mm wide and 0.23 mm thick (GE Medical Systems, Florence, SC). The thin niobium tin layer was sandwiched between two copper insulating layers, and the copper to noncopper ratio was 6:1.

The RF and gradient coils in conventional superconducting imagers completely surround the patient and preclude patient access in the same manner as that of the main magnet. Shielded gradient coils with a large central gap (56 cm) were developed for all three principal directions. These coils permitted access to the patient within the magnet bore without greatly reducing the gradient strength, linearity over the FOV, or eddy current performance (see Results). The acoustic noise generated by the gradient coils was measured by using a calibrated noise source (model S/N CA250-067; Larson-Davis Laboratories, Provo, Utah), a measuring amplifier and capacitive microphone (models 2609 and 2639, respectively; Bruel and Kjaer, Naerum, Denmark), and a spectrum analyzer (model 8568A; Hewlett-Packard, Palo Alto, Calif). RF signals were transmitted and received with the use of either a modified birdcage coil of conventional design (46) or surface coils operated in the transmit-receive mode. These surface coils could be integrated within a sterilized surgical drape and placed directly on the surface of the patient overlying the region to be imaged. The coils could be contoured to the patient's surface anatomy and permitted access to the region of treatment beneath the coil. In addition to flexible coils designed specifically for interventional procedures, it is expected that commercially available transmit-receive coils will be satisfactory in many applications.

The imager was installed in a specially constructed, magnetically shielded, hospital suite at the Brigham and Women's Hospital, Boston, Mass, for initial clinical evaluations. This interventional MR imaging facility was designed to provide the

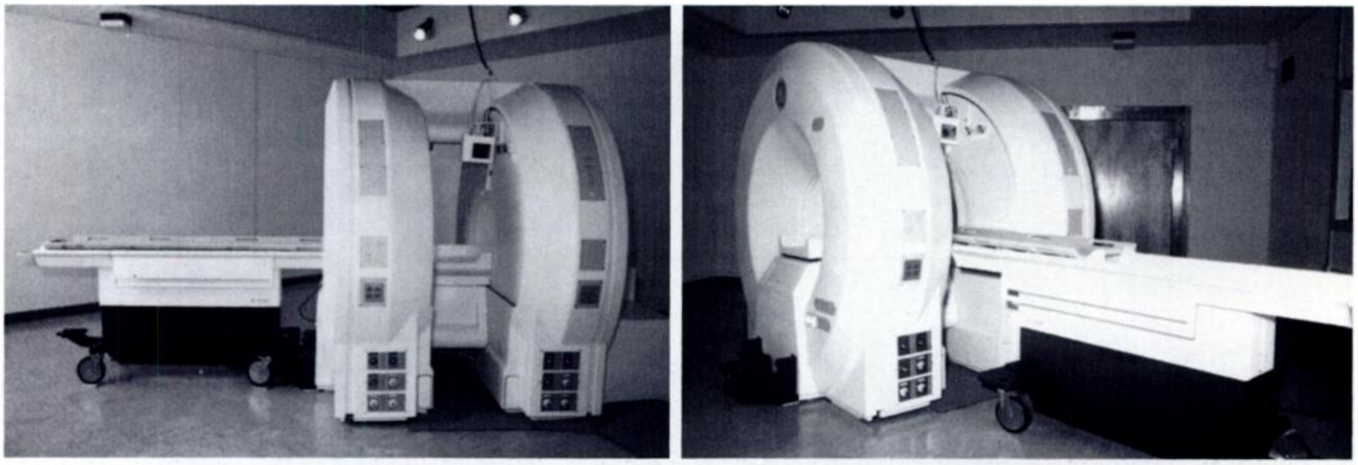

a. **b.**

Figure 1. Open-magnet system. Magnet is constructed by using two interconnected cryostats with an opening between them to permit clinical access to the patient during imaging. Depending on the procedure to be performed, the patient table may be positioned **(a)** along the axis of the imager or **(b)** perpendicular to this axis.

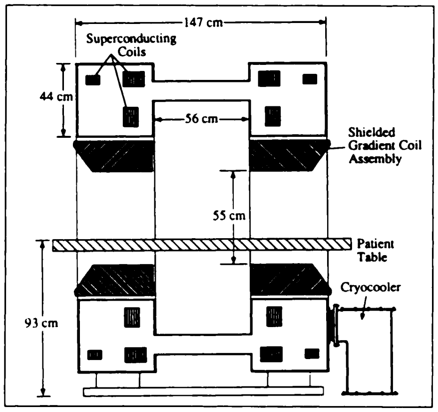

Figure 2. Cross-sectional diagram shows a magnet and gradient coil system, including approximate locations of superconducting coils.

combined features of MR imaging and interventional radiology as well as those of a conventional operating room. It includes an imaging room with the open magnet and its accessories along with MR-compatible equipment for administration of anesthetics (XL10 MRI Compatible Anesthesia Station; Ohmeda, Madison, Wis), patient monitoring devices (MagLife ODAM; Bruker, Wissembourg, France), video monitors, and two-way audiovisual communication devices. Service connections are provided for vacuum, air, and anesthetic gases, as well as for electrocautery, laser, and cryosurgical devices. Adjacent to the interventional imaging room are rooms for the imager console and for computer hardware. The rest of the suite contained the additional elements of an operating suite, such as decontamination and clean rooms for handling and assembling instruments, and a three-bed holding area for preoperative and postoperative care.

To permit interactive selection of the image plane, a three-dimensional digitizer system (Flashpoint; Pixsys, Boulder, Colo) was integrated into the system (Fig 3). This device employed three high-resolution video cameras to localize the spatial position of infrared light-emitting diodes, which could be mounted on rigid, handheld instruments. The position of the instrument tip within the patient could be determined from the position of two or more of the light-emitting diodes located outside the patient's body in the line of sight of the cameras. A specially programmed sequential logic box used the video images to calculate the probe orientation and the position vectors of the probe tip. An interactive workstation was developed to provide a software window environment that was capable of supporting mouse and menu-driven applications (Sun 4/670; Sun Microsystems, Mountain View, Calif). Instantaneous values for the instrument orientation and tip coordinates were calculated automatically by the workstation. These values could be used to control the MR image plane and imaging sequence directly from within the imager.

In some cases, it was desirable to use preoperative images for procedural planning and for advance preparation for the intraoperative imaging studies. In these cases, a three-dimensional imaging data set could be obtained from the patient before the procedure and transferred, with use of a database transfer program, to the computer workstation by means of Ethernet connections. Three-dimensional reconstructions and surface-rendering techniques could be used before the procedure for planning purposes, and the resulting images would be available during the procedure (47). Because the clinical team must be able to view the intraoperative images without leaving the imager, the display must operate within a strong magnetic field and cathode-ray tubes cannot be used. Therefore, a liquid crystal monitor with a viewing screen of 113.8 × 87.6 mm (model LQ6NC01; Sharp Electronics, Rahwah, NJ) was modified to remove magnetic field-sensitive ferrite components and was provided with additional shielding to prevent interference with the RF components of the MR imager. This monitor was mounted above the image region and permitted the viewing of the MR images as they became available. A second monitor facing in the opposite direction enabled an assistant across the patient table to view the images simultaneously.

RESULTS

Open-Magnet Performance and Patient Accessibility

The homogeneity of the main field was measured over a 30-cm-diameter spherical volume at the center of the magnet. The strength, linearity, eddy current, and acoustic properties of the gradient coils also were measured. The results are summarized in Table 2. The calculated gradient field pattern of the transverse gradient coils is indicated in Figure 4. The deviation from linearity was corrected during image reconstruction, as with standard imagers, by use of the mathematic expansion of the gradient field in a series of spherical harmonic functions.

The degree of clinical access to the patient is depicted ergonomically in Figure 5 for a male operator of median height (48). A chair with a built-in lumbar spine surface coil was developed to permit imaging of patients when they are in the sitting position (Fig 6). With this chair, it is possible to comfortably perform lumbar spine imaging on seated patients weighing up to 100 kg (220 lbs) and measuring 1.9 m (6 ft 3 inches) in height.

Image Quality

For construction of a superconducting MR imager with open access from

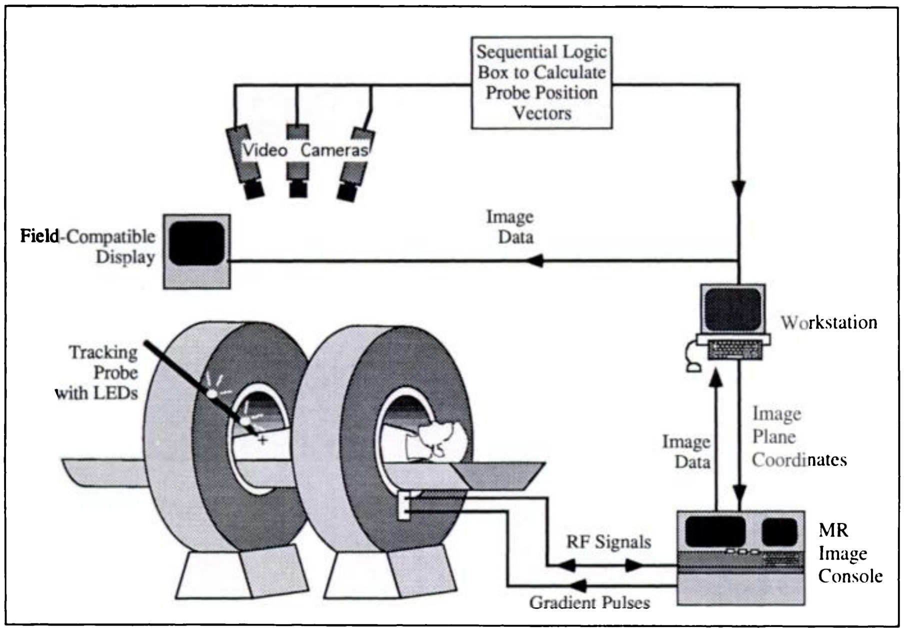

Figure 3. Schema of interactive image control shows an open-magnet design that permits direct clinical access to the patient and simultaneous control of the MR imaging process. Light-emitting diodes (*LEDs*) on the probes are visualized by the television cameras and allow calculation of the three-dimensional location of the probe tip. From within the magnet, the clinician can control the image plane and can view the resulting images on the field-compatible liquid crystal monitor.

Table 2
MR Imager Parameters

Parameter	Data
Main magnet	
Field strength	0.5 T
Homogeneity	12.3 ppm (30 cm DSV) 1.6 ppm (20 cm DSV) < 0.9 ppm (10 cm DSV)
Bore diameter	97 cm
Side-access opening	56 cm
Gradient system	
Gradient strength	8.0 mT/m (0.80 G/cm)
Inner diameter	55 cm
Side-access opening	56 cm
Deviation from linearity	≤1% (30 cm DSV)
Rise time*	0.933 msec
Gradient eddy currents (% of the applied gradient current)	< 0.05% (1 msec < τ < 10 msec) < 0.04% (10 msec < τ < 100 msec) < 0.02% (100 msec < τ < 1,950 msec)
Acoustic noise level	83 dB (high-power fast GRE pulse sequence)

Note.—DSV = diameter of spherical volume, GRE = gradient-recalled echo, τ = eddy current time constant.

* Time required to switch from zero gradient strength to full strength.

the side, it was necessary to make major adjustments to the position of the superconducting coils within the cryostat and to redesign all three gradient coils and the RF coils. Therefore, the ability of the imager to perform routine imaging tasks was an important test of the new main magnet and coil set. With the use of various pulse sequences, images of various anatomic regions were obtained with both birdcage head coils and several types of flexible surface coils tailored to specific anatomic regions (Fig 7). These devices operated in both the transmit and receive modes. Ideally, these coils should surround the point of entry into the body and produce minimal obstruction of the operating field. As with all surface coils, it was necessary to orient, as much as possible, the plane of these coils parallel to the main magnetic field to avoid loss of signal (49).

Qualitatively, it was found that within the 30-cm-diameter imaging region, this system possesses imaging capabilities comparable, or even slightly superior, to those of conventional 0.5-T MR imagers. This assessment was quantified by measuring the S/N, with use of identical phantoms, on the open-magnet MR imager and on a second 0.5-T MR imager with nearly identical receiver electronics (Signa Advantage; GE Medical Systems). With use of the same pulse sequences and head coil, the measured S/N of the open imager was 10% higher than that of the conventional imager. This advantage was attributed, at least in part, to the absence of a body coil in the open imager and the lack of associated noise coupling into the head coil.

Point-and-Image Capabilities and Real-Time Imaging

Systems for real-time MR data acquisition, reconstruction, and display have recently been demonstrated. In these cases, an interactive definition of the image plane is achieved either by entering parameters at a keyboard (50) or by graphic prescription from a scout image (51). In this system, the automatic, quantitative positional tracking of the light-emitting diodes on the Pixsys probe enables the clinician to prescribe images directly from within the magnet (Fig 3).

To perform an image-guided biopsy, the physician selected the images to be obtained by pointing the probe, which contained a coaxial biopsy needle, in the direction of the tissue target within the patient. The coordinates of the needle tip and a unit vector along the projected track of the needle, were calculated by the workstation and relayed to the imager console. An image in a plane containing the needle path was acquired automatically and displayed on the monitor within the imager. If the image helped confirm an appropriate orientation of the biopsy needle, the needle could be advanced to the target while its progress was monitored by repetitively updated images. If the orientation of the biopsy needle was unsatisfactory, the probe could be redirected and additional images obtained until a satisfactory approach

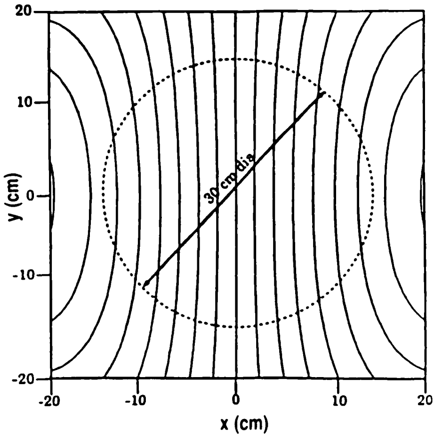

Figure 4. Field pattern for transverse gradient coils with open geometry. Patterns of transverse and axial gradient fields are similar. The boundary of a 30-cm-diameter (*dia*) sphere is indicated.

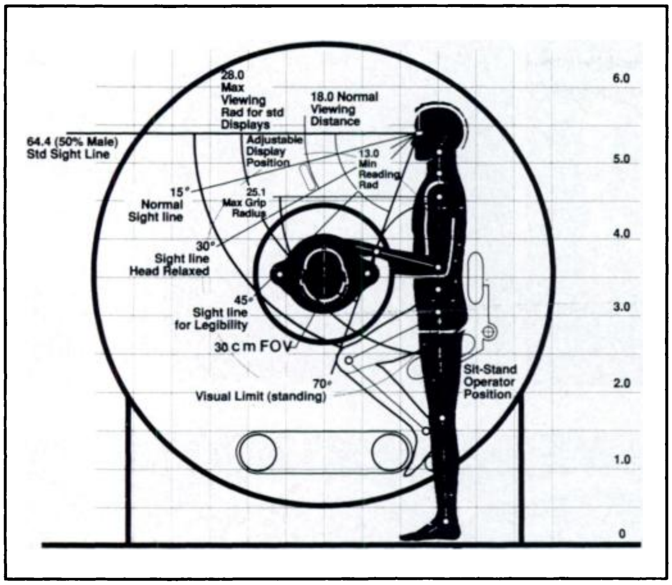

5a.

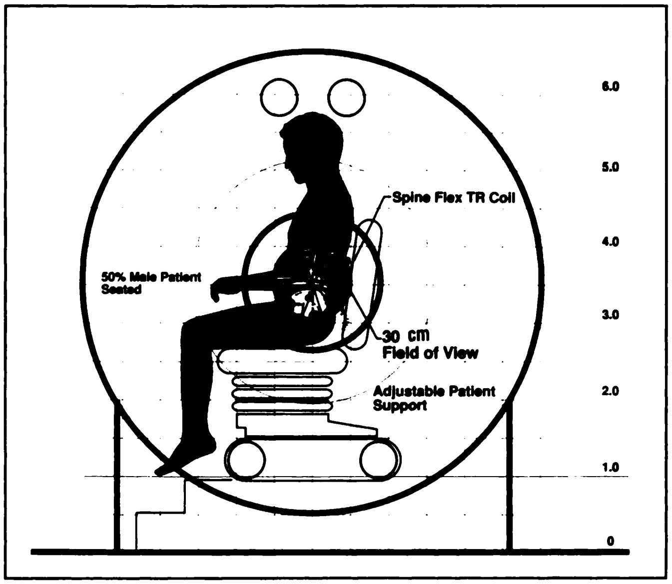

6a.

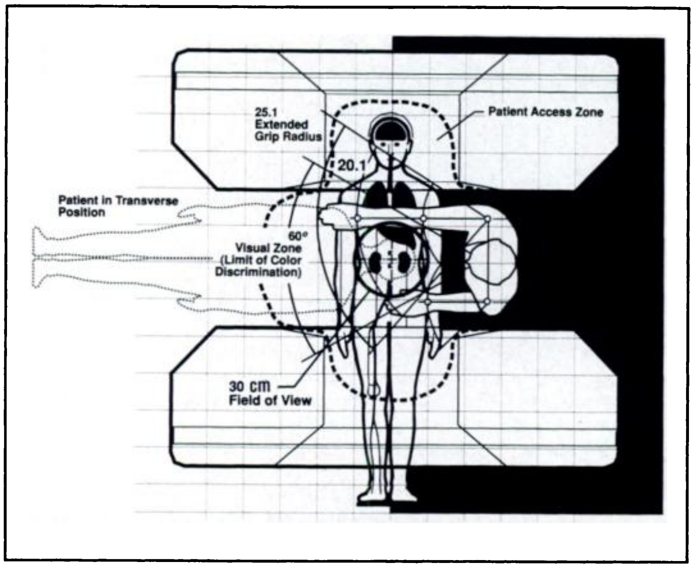

5b.

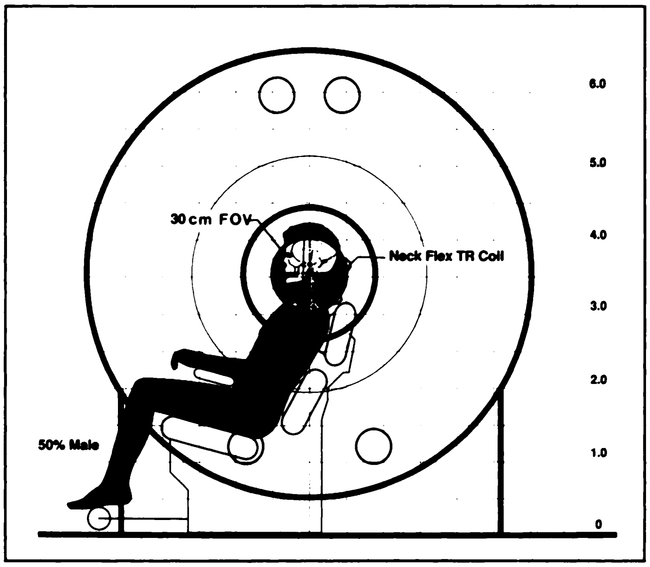

6b.

Figures 5, 6. **(5)** Clinical access and working zones. Effective MR imaging is possible over a spherical volume, at the center of the magnet, approximately 30 cm in diameter. The clinician may stand or sit at the patient's side or head. Regions of the patient accessible to the vision and reach for a male operator of median height (48) are shown, in inches, for the **(a)** vertical and **(b)** horizontal planes. Values on the y axis are in feet. **(6)** Patient positioning options. Unlike conventional superconducting systems, spine images may be obtained in patients who are upright. Values on the y axis are in feet. TR = repetition time. **(a)** Lumbar spine may be imaged with the patient seated. It is also possible to image this region with the patient standing. **(b)** If the sitting position is lowered, the cervical spine may also be imaged with the patient upright.

to the target was determined. If desired, image planes perpendicular to the needle path could also be prescribed. The speed of imaging was important because it was necessary to produce clinically useful images while causing only minimal delays in the procedure.

With the use of fast GRE sequences, it was possible with this imager to produce images useful for guiding the biopsy of large masses (8-cm FOV, 128 × 256 matrix, 5-mm-section thickness) at the rate of one image every 1.5 seconds (Figs 8, 9). Under protocols approved by our Institutional Review Board, initial MR-guided biopsies were performed in patients (52) by using this system (Fig 10). With this GRE pulse sequence, the magnetic susceptibility of the needle produced an imaging void that was several times the actual size of the needle, which has a diameter of 1.24 mm. When a biopsy specimen of a large mass was obtained, this artifact was acceptable and was possibly even useful for guidance of the instrument (16). However, for application of this technique to smaller masses, biopsy needles with better magnetic susceptibility matches to tissue are necessary.

Positional Accuracy of Pixsys-based Imaging

In principle, the ability of MR imaging to determine spatial localization is limited only by the pixel size and thickness of the imaged section, and localization within 1 mm or less is theoretically possible (53,54). However, because of several systematic sources of error, this level of positional accuracy has not yet been achieved for this system. These factors included (*a*) errors in the calculated gradient fields, which remained even after mathematic corrections were

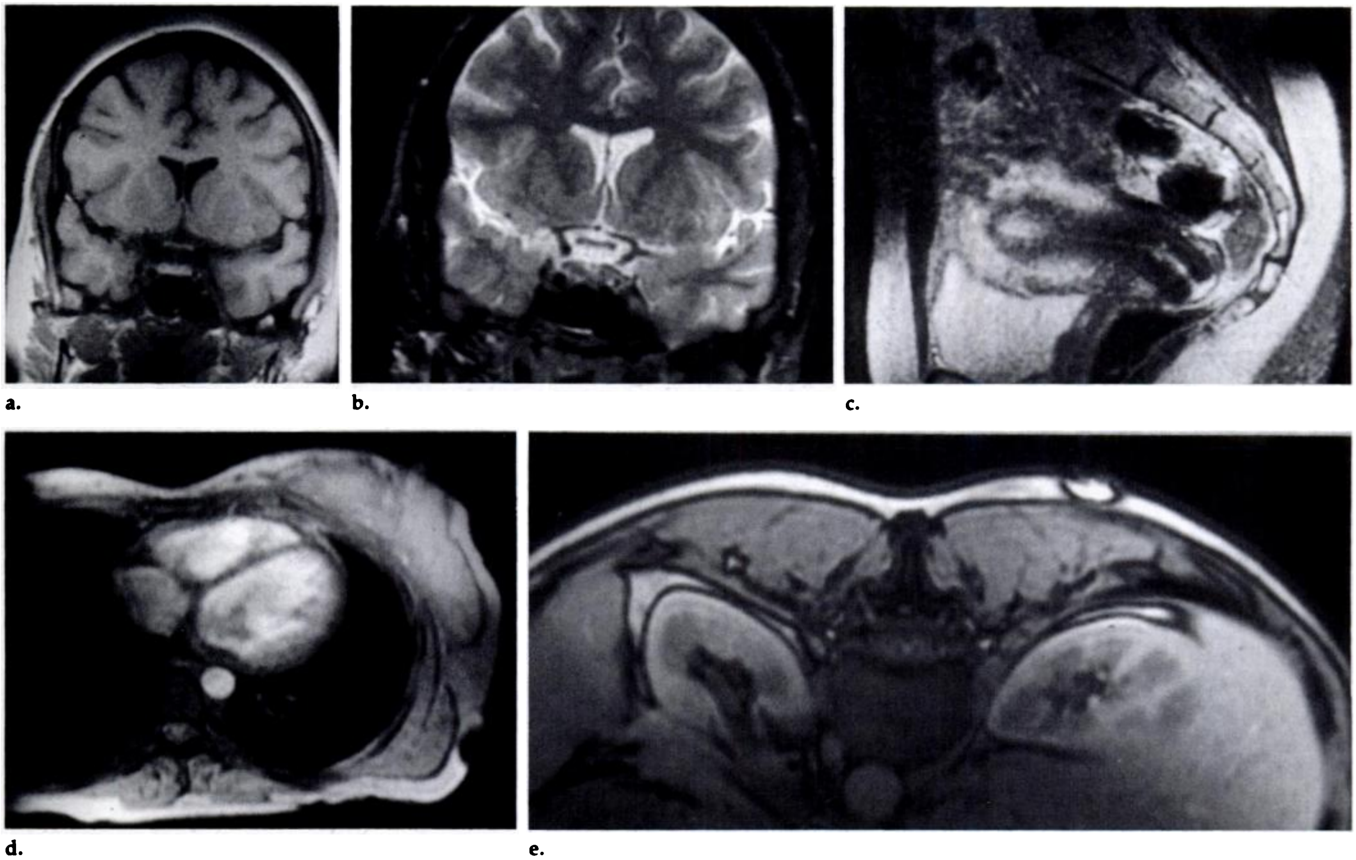

Figure 7. Images obtained by using the open-configuration MR imager show that, despite radical modifications of the superconducting magnet and the RF and gradient coils, high-quality anatomic imaging can be achieved. **(a)** T1-weighted spin-echo MR image (550/25 [repetition time msec/echo time msec]) of the patient's head was obtained with a section thickness of 5 mm, FOV of 22 × 16 cm, 256 × 192 matrix, two acquisitions, an imaging time of 2 minutes 42 seconds, and use of a conventional birdcage head coil. System homogeneity also permitted T2-weighted fast spin-echo MR images of the **(b)** head (4,000/88, 5-mm section thickness, 20-cm FOV, 256 × 192 matrix, two acquisitions, imaging time of 3 minutes 12 seconds) and **(c)** female pelvic organs (3,000/88, 7-mm section thickness, 24-cm FOV, 256 × 256 matrix, two acquisitions, imaging time of 3 minutes 18 seconds), both with use of flexible surface coils. GRE and flexible surface coils were used to obtain a **(d)** cardiac cine mode image (80/18, 7-mm section thickness, 32-cm FOV, 256 × 128 matrix, four acquisitions, 30° flip angle, imaging time of 8 minutes 6 seconds) and an **(e)** axial abdominal T1-weighted MR image (150/8.3, 10-mm section thickness, 26-cm FOV, single acquisition, 80° flip angle, imaging time of 45 seconds).

made, and (*b*) deviations from purely planar imaging surfaces (potato chip effect). The magnetic susceptibility of the human tissues and of any instruments introduced into the imaging field resulted in geometric image distortions (55,56). Other factors included the positional accuracy of the Pixsys and the accuracy of the registration between the coordinate systems of the imager and of the Pixsys device. Further work is necessary to reduce positional errors by use of more powerful mathematic corrections for field distortions, pulse sequences that are relatively less sensitive to field distortions (57,58), and instruments that have magnetic susceptibilities closely matched to human tissues.

The Pixsys device and the MR imager each develops positional information referenced to its own three-dimensional coordinate system, and a mathematic transformation was necessary to relate data between these two systems. This transformation was generated by registering an array of standard positions, which are measured in both frames of reference. The overall positional accuracy depended on the accuracy of the individual components of the imaging system and was determined by the accuracy of the following: the probe tip location and direction, as determined in the Pixsys coordinate system; the tissue target location within the image; and the determination of the transformation function and standard positions.

The positional accuracy and repeatability of the Pixsys Flashpoint digitizer were studied by mounting the video cameras 1 m above a simulated imaging volume. The coordinates produced by the digitizer were compared with those of a three-dimensional, computer-controlled micrometer stage. Three reference points were measured to register the coordinate systems of the Pixsys and the micrometer stage. The repeatability and accuracy of the probe were greatest when it was oriented perpendicular to the line of sight of the video cameras. With use of this orientation,

Figure 8. Real-time imaging is achieved by updating the MR image every 1.5 seconds. An oblique image plane along the direction of a biopsy cannula can be selected automatically by the operator using the position-sensing instruments and software shown in Figure 3. The graphic overlay indicates the orientation of the cannula and its projected extension into the patient. Part of the operator's hand is seen posterior to the patient in a single-acquisition, GRE image (14.9/7.1, 10-mm section thickness, 30-cm FOV, 30° flip angle, 256 × 128 matrix, imaging time of 1.5 seconds).

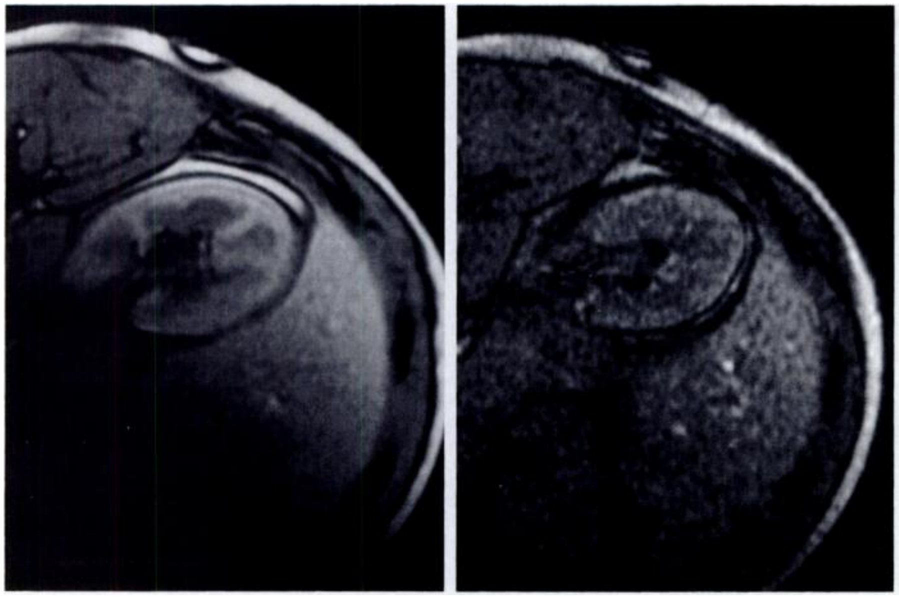
a. b.

Figure 9. Effect of imaging time is demonstrated by comparison of axial GRE images obtained by using flexible surface coils at comparable lumbar levels. Both images have a 20-cm FOV, a 256 × 128 matrix, and an 80° flip angle. **(a)** T1-weighted image (100/8.8, 8-mm section thickness, two acquisitions) requires a total imaging time of 58 seconds. **(b)** As expected, an MR image of an adjacent region obtained with use of a real-time single-acquisition sequence (16/7.8, 10-mm section thickness) that requires only 1.5 seconds has a lower S/N but contains sufficient anatomic detail for many interventional procedures.

a group of locations was measured repetitively, producing a total of 4,000 position coordinates. The range of these results was ±0.3 mm with a standard deviation of 0.1 mm. Subsequently, the probe tip was fixed in position and the probe handle was rotated to study the accuracy of the transformation between the two sets of coordinate systems. The range of these measurements was ±3.0 mm with a standard deviation of 1.0 mm. The largest errors occurred when the angle between the probe and the camera line of sight was less than approximately 10°; in practice, this probe orientation should be avoided. The absolute accuracy of the Pixsys device was studied by measuring the coordinates of 44,100 points as a computer-controlled micrometer stage moved the probe through a series of locations within an 18-cm-diameter spherical volume. The initial measurements produced a mean positional error of 2.79 mm with a standard deviation of 1.2 mm. The errors were found to increase with the distance from the origin. By recalculating the registration transformation based on the measurements, the mean error was reduced to 1.0 mm with a standard deviation of 0.5 mm.

An additional factor in the overall system accuracy was the precision with which an image plane could be specified. This was measured by mounting the Pixsys on a three-axis positioner, which permitted it to be moved throughout the imaging region. A 9-mm-diameter glass sphere that contained copper sulfate solution was mounted on the probe tip. Three mutually perpendicular capillary tubes, 1 mm in diameter and filled with copper sulfate solution, were used as a crosshair phantom, which was carefully positioned until it was aligned at the center of the magnet coordinate system. This was determined by successive images in the axial, coronal, and sagittal planes. With the probe aligned along the axial direction of the imager, it was moved to various locations within and also, somewhat beyond, the 30-cm-diameter spherical volume. At each location, it was used interactively to generate axial, sagittal, and coronal images through the sphere at the probe tip. The center coordinates of the image of the copper sulfate sphere were measured in each image. Nominally, the sphere should be centered at the center pixel of each image. The actual position of the center of the sphere (δx, δy, δz) in the images was determined in the image coordinate system. This gave six measured offset values: two (δx and δy) in the axial image, two (δy and δz) in the sagittal image, and two (δx and δz) in the coronal image. The three pairs of coordinate offsets were compared, and the larger of each pair was considered the offset error for that coordinate direction. By using the larger value of each of the three pairs, the total error in the location of the image plane was taken as $(\delta x^2 + \delta y^2 + \delta z^2)^{1/2}$. The mean error in the location of the center pixel of the image plane was 2 mm near the center of the imager and was found to increase, as expected, with distance from the magnet isocenter (Table 3).

Instrument Tracking with Use of MR Signals

In addition to the Pixsys-based localization techniques, a device tracking technique with a function analogous to x-ray fluoroscopy but based on MR data was integrated with this system (59). This arrangement used pulsed gradient fields and was applicable to real-time monitoring of the position of either rigid or flexible devices (needles, catheters, tubes, drains, rigid or flexible endoscopes) used in a patient. The tracking of fiducial locations (such as a catheter tip) on these invasive devices was made possible by incorporation of one or more small (diameter < 1 mm) receiver coils into the device. These small coils helped detect MR signals only from the immediately adjacent tissues. Pulse sequences that used nonselective RF pulses from the standard transmitter coils were used to excite all of the spins within the FOV. The tracking coils produced no substantial RF tissue heating because they were used only to receive, not to transmit, RF energy. Readout magnetic field gradient pulses, typically applied along one of the primary axes of the imaging system, were used to frequency-encode the position of the receiver coil or coils. The data are Fourier transform, and the spectral peak was used to determine the location of each receiver coil along the direction of the readout gradient. Subsequent data, collected on orthogonal axes, permitted three-dimensional localization of the small coils. These coordinates could be computed rapidly, and the position of each coil could be updated several times per second. The precision of the RF coil localization was limited by its size but was comparable to the pixel size of the conventional image. The robustness of the tracking algorithm was limited by the S/N of the voltage received from the RF coil. In principle, if this coil is aligned with its axis parallel to the main magnetic field, no MR signal is detected. However, this was not

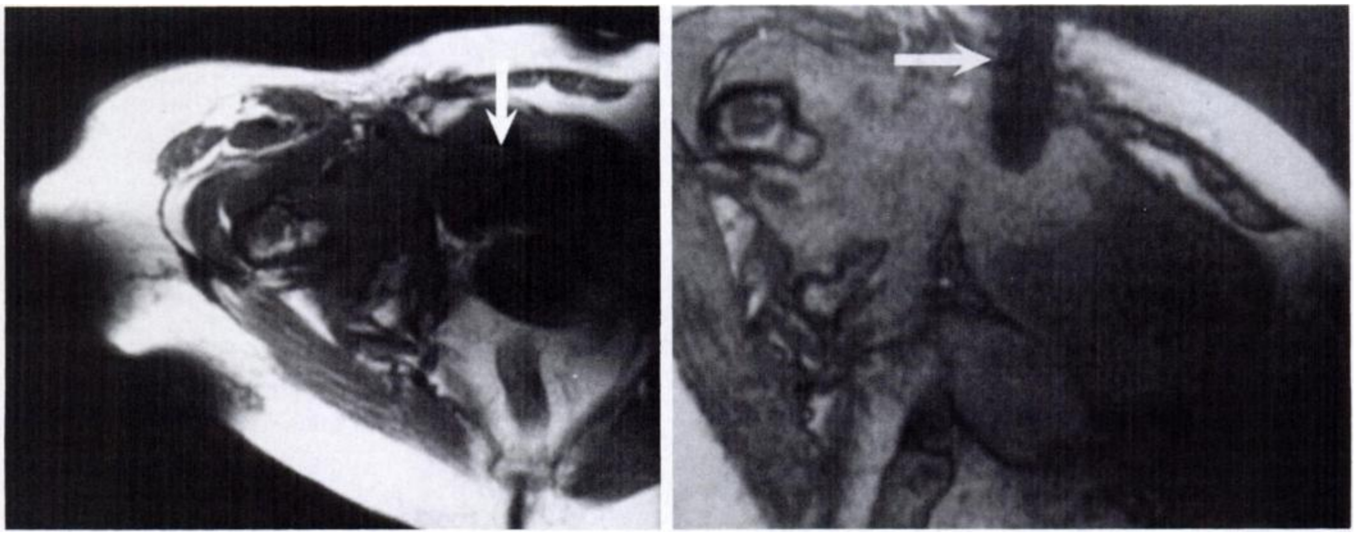

Figure 10. MR images obtained at biopsy of a pelvic mass (malignant schwannoma), extending to the urinary bladder, guided by the open-configuration MR imaging system. **(a)** T1-weighted spin-echo images (600/25, 10-mm section thickness, 26-cm FOV, 256 × 192 matrix, two acquisitions, imaging time of 3 minutes 54 seconds) obtained with a flexible surface coil shows a mass (arrow) of intermediate signal intensity in the right groin, extending to and involving the right bladder wall. **(b)** One of a series of real-time, T2*-weighted, GRE MR images obtained interactively every 1.5 seconds (16/7.7, 10-mm section thickness, 24-cm FOV, 256 × 128 matrix, single acquisition, 30° flip angle) shows an 18-gauge MR-compatible biopsy needle (E-Z-Em, Westbury, NY) advanced into the mass (arrow).

a problem in practice because the coil could be detected with very low S/N and could be easily detected except for a very small range of orientations.

The coil-localization pulse sequence was interleaved with a conventional imaging sequence, and the coil position was displayed as a graphic symbol superimposed on the conventional image. Registration of the device location with the patient anatomy on this combined image was excellent because the same principles and hardware were used for both computations and any positional errors caused by nonlinearities of the readout gradient were identical for both the anatomic and device coordinates. In future applications, it may be desirable to register the position of the RF coil to stereotaxic coordinates referenced to an external reference frame. In this case, positional errors between the MR tracking coordinates and the external frame of reference need to be determined and considered.

Safety Considerations

The imager was designed to meet all regulations from the Food and Drug Administration and other regulatory bodies (60,61) that are applicable to MR imaging. The values for the gradient strength and rise time (Table 2) were chosen such that the maximum rate of change of the gradient field, dB/dt, was less than the limit approved by the Food and Drug Administration (60) of 20 T/sec at all locations within the imager that were accessible to the patient and the clinical staff. The acoustic noise was substantially muted by the use of epoxy-filled gradient coil forms. These levels were measured during the continuous running of a fast GRE sequence (one image every 1.5 seconds), which represents the highest energy pulse sequence available on the imager. The background sound level in the image room was 70 dB and was produced mainly by the cryocooler assembly. The maximum sound level (A-weighted) during imaging at locations measured next to the gradient coils and at the ear-level positions of patients and staff was 82–83 dB. The Occupational Safety and Health Administration standard for 8 hours of continual noise exposure was 90 dB on this scale (60,62).

An RF power monitor, identical to that used on commercial 0.5-T imagers, was used to keep the whole-body specific absorption rate (SAR) below the limit set by the Food and Drug Administration. To meet these requirements, infants who weighed less than 9 kg could not be imaged without specific Institutional Review Board approval. For protection against the possibility of cold burns, all cryogenic fittings and cold surfaces were covered and made inaccessible to patients and staff. Ferromagnetic instruments and components were excluded from the imaging room to avoid image artifacts and the dangers associated with their unplanned movement or dislodgment. Care also was taken with instruments containing conducting metallic components. Through the Faraday law of induction, closed-loop conducting paths interact with the RF fields (and to some extent with the switched gradient fields) and can produce image artifacts and potentially dangerous electric currents and arcing (63,64). Extensive experience with metallic implants (61) has shown that, as expected, small, nonferromagnetic, metallic conductors that do not form closed loops may be imaged without danger. Clinical instrumentation that is adapted for use in this setting is required to have ferromagnetic components replaced with nonmagnetic materials and, to the extent feasible, electrical conductors, such as metals, replaced with nonconductors.

Table 3
Positional Errors in Image Plane Selection

Distance from Magnet Isocenter (cm)	No. of Locations Measured	Error (mm) Mean	Error (mm) Maximum
0	1	2.2	2.2
5	6	2.6	3.8
10	6	2.9	4.6
15	12	3.2	5.8
18	8	5.2	6.7

DISCUSSION

Each imaging modality has certain limitations when used for image-guided therapy. Direct visualization, video monitoring, and endoscopy are limited to inspection of exposed surfaces. X-ray fluoroscopy provides real-time monitoring but provides only projection images and, because of the poor definition of soft tissues, target definition is limited. CT provides good soft-tissue definition and three-dimensional localization but is not sufficiently sensitive to monitor or control tissue temperature. In addition, all x-ray-based systems involve ionizing radiation, and their use for continuous monitoring is restricted. Diagnostic US provides real-time imaging and can follow the trajectory of interventional devices, but the tissue characterization and the ability to monitor and control energy deposition are limited.

In many respects, MR imaging is ideally suited to provide imaging guidance for the wide range of minimally invasive procedures now under development. Advantages of MR imaging include good spatial resolution with excellent soft-tissue discrimination; sensitivity to blood flow, perfusion, and temperature; lack of ionizing radiation; ability to image planes of any orientation; and the recent development of fast and ultrafast imaging techniques that permit rapid, repeated imaging.

However, the use of intraoperative MR imaging has been limited by the inaccessibility of the patient and by the time required to determine proper imaging planes, to enter this information at the MR imaging console, and to complete the preimaging protocols. This sluggishness has made it difficult to conceive that MR imaging could keep pace with typical interventional procedures.

The MR imager described in this report overcomes this difficulty by permitting interactive image control and near real-time imaging rates. These advantages, along with the ability to maintain continuous direct contact with the patient, increase the range of procedures for which MR guidance may be useful.

Further work is needed to enhance the positional accuracy of the system, to confirm the safety of members of the clinical team who will experience long-term exposure to the MR imaging environment, and to develop appropriate treatment protocols. New, interdepartmental approaches to the use of such systems may be needed. An extensive investigational program is necessary to define the ultimate clinical role of this technique. This program is under way, with the goals of enhancing patient outcomes and reducing the overall cost of interventional treatments. ■

Acknowledgments: It is a pleasure to acknowledge the important contributions of many colleagues: Mark E. Vermilyea, PhD, Kenneth G. Herd, PhD, Charles J. Rossi, Jr, Ralph Hashoian, BS, William J. Adams, MS, Scott M. Yohe, BA, Raymond E. Argersinger, J. Arlene Agresta, Randy O. Giaquinto, Howard Lilly, MS, Michele Ogle, MS, Erika Schneider, PhD, Anton M. Linz, MS, H. Glenn Reynolds, MS, Edward M. Kerwin, BS, Robert B. Lufkin, MD, Daniel J. Castro, MD, George P. Topulos, MD, Eben Alexander III, MD, Marvin P. Fried, MD, P. Langham Gleason, MD, Krishna Kandarpa, MD, PhD, and Samuel Singer, MD.

References

1. Jolesz FA, Shtern F. The operating room of the future: report of the National Cancer Institute Workshop—imaging-guided stereotactic tumor diagnosis and treatment. Invest Radiol 1992; 27:326–328.
2. Mueller PR, Stark DD, Simeone JF, et al. MR-guided aspiration biopsy: needle design and clinical trials. Radiology 1986; 161:605–609.
3. Herman SD, Friedman AC, Radecki PD, Caroline DF. Incidental prostatic carcinoma detected by MRI and diagnosed by MRI/CT-guided biopsy. AJR 1986; 146:351–352.
4. Lufkin R, Teresi L, Chiu L, Hanafee W. A technique for MR-guided needle placement. AJR 1988; 151:193–196.
5. Lufkin R, Duckwiler G, Spickler E, et al. MR body stereotaxis: an aid for MR guided biopsies. J Comput Assist Tomogr 1988; 12:1088–1089.
6. Duckwiler G, Lufkin RB, Teresi L, et al. Head and neck lesions: MR-guided aspiration biopsy. Radiology 1989; 170:510–522.
7. To SYC, Lufkin RB, Chiu L. Technical note: MR compatible winged infusion set. Comput Med Imaging Graph 1989; 13:469–472.
8. Hu X, Tan KK, Levin DN, et al. Three-dimensional magnetic resonance images of the brain: application to neurosurgical planning. J Neurosurg 1990; 72:433–440.
9. Heilbrun MP, McDonald P, Wilker C, et al. Stereotactic localization and guidance using a machine vision technique. Stereotact Funct Neurosurg 1992; 58:94–98.
10. Wenokur R, Andrews JC, Abemayor E, et al. Magnetic resonance imaging-guided fine needle aspiration for the diagnosis of skull base lesions. Skull Base Surg 1992; 2:167–170.
11. Hathout G, Lufkin RB, Jabour B, Andrews J, Castro D. MR-guided cytology in the head and neck at high field strength. JMRI 1992; 2:93–94.
12. Ehricke HH, Schad, LR, Gademan G, Wowra B, Englehart R, Lorenz J. Use of MR angiography for stereotactic planning. J Comput Assist Tomogr 1992; 16:35–40.
13. Pitt AM, Fleckenstein JL, Greenlee RG, Burns DK, Bryan WW, Haller R. MRI-guided biopsy in inflammatory myopathy: initial results. Magn Reson Imaging 1993; 11:1093–1099.
14. Fried MP, Jolesz FA. Image-guided intervention for diagnosis and treatment of disorders of the head and neck. Laryngoscope 1993; 103:924–927.
15. Jolesz FA, Blumenfeld M. Interventional use of magnetic resonance imaging. Mag Reson Q 1994; 10:85–96.
16. Silverman SG, Lorensen WE, Kikinis R, et al. MR-guided biopsy in an open configuration interventional MR imaging system (abstr). Radiology 1994; 193(P):268–269.
17. Kooy HM, van Herk M, Barnes PD, et al. Image fusion for stereotactic radiotherapy and radiosurgery treatment planning. Int J Radiat Oncol Biol Phys 1994; 28:1229–1234.
18. Jolesz FA, Bleier AR, Jakab P, Ruenzel PW, Huttl K, Jako GJ. MR imaging of laser tissue interactions. Radiology 1988; 168:249–253.
19. Bleier AR, Higuchi N, Panych LP, Jakab PD, Hrovat M, Jolesz FA. Magnetic resonance imaging of interstitial laser photocoagulation. Proc SPIE 1990; 1202:188–195.
20. Higuchi N, El Azouzi M, Black PM, Moore MR, Hsu D, Jolesz FA. The use of MRI-guided interstitial laser surgery in experimental brain tumors (abstr). Magn Reson Imaging 1990; 8(suppl 1):94.
21. Bleier, AR, Jolesz FA, Cohen MS, et al. Real-time magnetic resonance imaging of laser heat deposition in tissue. Magn Reson Med 1991; 21:132–137.
22. Anzai Y, Lufkin R, Castro D, et al. MR imaging-guided interstitial Nd:YAG laser phototherapy: dosimetry study of acute tissue damage in an ex vivo model—dosimetry of laser-MR-tissue interaction. JMRI 1991; 1:553–559.
23. Anzai Y, Lufkin RB, Saxton RE, et al. Nd:YAG interstitial laser phototherapy guided by magnetic resonance imaging in an ex vivo model: dosimetry of laser-MR-tissue interaction. Laryngoscope 1991; 101:755–760.
24. Bettag M, Ulrich F, Kahn T, Switz R. Local interstitial hyperthermia in malignant brain tumors using a low power Nd:YAG laser. Proc SPIE 1991; 1525:409–411.
25. Fan M, Ascher PW, Schrottner O, Ebner F, Germann RH, Kleinert R. Interstitial 1.06 Nd:YAG laser thermotherapy in malignant gliomas under real-time monitoring of MRI: experimental studies and phase I clinical trial. J Clin Laser Med Surg 1992; 10:355–361.
26. Matsumoto R, Jolesz FA, Selig AM, Colucci VM. Interstitial Nd:YAG laser ablation in normal rabbit liver: trial to maximize the size of laser-induced lesions. Lasers Surg Med 1992; 12:650–658.
27. Tracz RA, Wyman DR, Little PB, et al. Comparison of magnetic resonance images and histopathological findings of lesions induced by interstitial laser photocoagulation in the brain. Lasers Surg Med 1993; 13:45–54.
28. Gewiese B, Beuthan J, Fobbe F, et al. Magnetic resonance imaging-controlled laser-induced interstitial thermo-therapy. Invest Radiol 1994; 29:345–351.
29. Matsumoto R, Mulkern RV, Hushek SG, Jolesz FA. Tissue temperature monitoring for thermal interventional therapy: a comparison of T1-weighted MR pulse sequences. JMRI 1994; 4:65–70.
30. Gilbert JC, Rubinsky B, Roos MS, Wong STS, Brennan KM. MRI-monitored cryosurgery in the rabbit brain. Magn Reson Imaging 1993; 11:1155–1164.
31. Matsumoto R, Selig AM, Colucci VM, Jolesz FA. MR monitoring during cryotherapy of the liver: predictability of histological outcome. JMRI 1993; 3:770–776.
32. Jolesz FA, Jakab PD. Acoustic pressure wave generation within a magnetic resonance imaging system: potential medical applications. JMRI 1991; 1:609–613.
33. Hynynen K, Darkazanli A, Unger E, Schenck JF. MRI-guided noninvasive ultrasound surgery. Med Phys 1992; 20:107–116.

34. Cline HE, Schenck JF, Hynynen K, Watkins RD, Souza SP, Jolesz FA. MR-guided focused ultrasound surgery. J Comput Assist Tomogr 1992; 16:956–965.
35. Hynynen K, Damianou C, Darkazanli A, Unger E, Schenck JF. The feasibility of using MRI to monitor and guide noninvasive ultrasound surgery. Ultrasound Med Biol 1993; 19:91–92.
36. Cline HE, Schenck JF, Watkins RD, Hynynen K, Jolesz FA. Magnetic resonance-guided thermal surgery. Magn Reson Med 1993; 30:98–106.
37. Cline HE, Hynynen K, Watkins RD, et al. Focused US system for MR imaging–guided tumor ablation. Radiology 1995; 194:731–737.
38. Soper NJ, Brunt LM, Kerbl K. Laparoscopic general surgery. N Engl J Med 1994; 330:409–413.
39. Thomas SR. Magnets and gradient coils: types and characteristics. In: Bronskill MJ, Sprawls P, eds. The physics of MRI: medical physics monograph no. 21. Woodbury, NY: American Institute of Physics, 1993; 56–97.
40. Kaufman L, Arakawa M, Hale J, et al. Accessible magnetic resonance imaging. Magn Reson Q 1989; 5:283–297.
41. Gronemeyer DH, Kaufman L, Rothschild P, Seibel RM. New possibilities and aspects of low-field magnetic resonance tomography. Radiol Diagn 1989; 30:519–527.
42. Laskaris ET, Ackermann R, Dorri B, Gross D, Herd K, Minas C. A cryogen-free open superconducting magnet for interventional MRI applications. IEEE Trans Appl Superconductivity 1995 (in press).
43. Wilson MN. Superconducting magnets. Oxford, England: Clarendon, 1983; 279–310.
44. Benz MG. Superconducting properties of diffusion processed niobium-tin tape. IEEE Trans Magnetics 1966; 2:760–764.
45. Benz MG, Rumaner LE, Knudsen BA, Zabala RJ, Hart HR Jr. Melt-formed superconducting joints for Nb_3Sn tape. J Electronic Materials 1993; 22:1299–1303.
46. Hayes CE, Edelstein WA, Schenck JF, Mueller OM, Eash M. An efficient, highly homogeneous radiofrequency coil for whole-body NMR imaging at 1.5T. J Magn Reson 1985; 63:622–628.
47. Jolesz FA, Lorensen WE, Kikinis R, et al. Virtual endoscopy: three-dimensional rendering of cross-sectional images for endoluminal visualization (abstr). Radiology 1994; 193(P):469–470.
48. Diffrient N, Tilley AR, Bardagjy JC, eds. Humanscale 1/2/3. Cambridge, Mass: MIT Press, 1974; 4–23.
49. Schenck JF, Hart HR Jr, Foster TH, Edelstein WA, Hussain MA. High resolution magnetic resonance imaging using surface coils. In: Kressel HY, ed. Magnetic resonance annual. New York, NY: Raven, 1986; 123–160.
50. Holsinger AE, Wright RC, Riederer SJ, Farzaneh F, Grimm RC, Maier JK. Real-time interactive MR imaging. Magn Reson Med 1990; 14:547–553.
51. Hardy CJ, Darrow RD, Nieters EJ, et al. Real-time acquisition, display, and interactive graphic control of NMR cardiac profiles and images. Magn Reson Med 1993; 29:667–673.
52. Jolesz FA, Silverman SG, Kikinis R, et al. Interactive image-guided interventions in an open-configuration MR imaging system (abstr). Radiology 1994; 193(P):252.
53. Kondziolka D, Dempsey PK, Lunsford LD, et al. A comparison between magnetic resonance imaging and computed tomography for stereotactic coordinate determination. Neurosurgery 1992; 30:402–407.
54. Sumanaweera TS, Adler JR, Napel S, Glover GH. Characterization of spatial distortion in magnetic resonance imaging and its implications for stereotactic surgery. Neurosurgery 1994; 35:696–704.
55. Lüdeke KM, Röschmann P, Tischler R. Susceptibility artifacts in MR imaging. Magn Reson Imaging 1985; 3:329–343.
56. Czervionke LF, Daniels DL, Wehrli FW, et al. Magnetic susceptibility artifacts in gradient-recalled echo MR imaging. Am J Neuroradiol 1988; 9:1145–1155.
57. Chang H, Fitzpatrick JM. A technique for accurate magnetic resonance imaging in the presence of field inhomogeneities. IEEE Trans Med Imaging 1992; 11:319–329.
58. Sumanaweera TS, Glover GH, Binford TO, Adler JR. MR susceptibility misregistration correction. IEEE Trans Med Imaging 1993; 12:251–259.
59. Dumoulin CL, Souza SP, Darrow RD. Real-time position monitoring of invasive devices using magnetic resonance. Magn Reson Med 1993; 29:411–415.
60. Shellock FG, Kanal E. Magnetic resonance bioeffects, safety, and patient management. New York, NY: Raven, 1994; 19–40.
61. Shellock FG, Morisoli S, Kanal M. MR procedures and biomedical implants, materials, and devices: 1993 update. Radiology 1993; 189:587–599.
62. Hurwitz R, Lane SR, Bell RA, Brant-Zawadzki MN. Acoustic analysis of gradient-coil noise in MR imaging. Radiology 1989; 173:545–548.
63. Schenck JF. Phase-encoding artifacts produced by open loop metallic conductors within the field-of-view (abstr). In: Proceedings of the Society of Magnetic Resonance 1994. Berkeley, Calif: Society of Magnetic Resonance, 1994; 220.
64. Camacho CR, Plewes DB, Henkelman RM. Non-susceptibility artifacts due to metallic objects in MRI. JMRI 1995; 5:75–88.